PHYSICAL REVIEW MATERIALS **2**, 023605 (2018)

Fracture of coherent interfaces between an fcc metal matrix and the $Cr_{23}C_6$ carbide precipitate from first principles

Elric Barbé,[1,2] Chu-Chun Fu,[1] and Maxime Sauzay[2]

[1]*DEN-Service de Recherches de Métallurgie Physique, CEA, Université Paris-Saclay, F-91191 Gif-sur-Yvette, France*

[2]*DEN-Service de Recherches Métallurgiques Appliquées, CEA, Université Paris-Saclay, F-91191 Gif-sur-Yvette, France*

(Received 22 December 2017; published 27 February 2018)

It is known that microcrack initiation in metallic alloys containing second-phase particles may be caused by either an interfacial or an intraprecipitate fracture. So far, the dependence of these features on properties of the precipitate and the interface is not clearly known. The present study aims to determine the key properties of carbide-metal interfaces controlling the energy and critical stress of fracture, based on density functional theory (DFT) calculations. We address coherent interfaces between a fcc iron or nickel matrix and a frequently observed carbide, the $M_{23}C_6$, for which a simplified chemical composition $Cr_{23}C_6$ is assumed. The interfacial properties such as the formation and Griffith energies, and the effective Young's modulus are analyzed as functions of the magnetic state of the metal lattice, including the paramagnetic phase of iron. Interestingly, a simpler antiferromagnetic phase is found to exhibit similar interfacial mechanical behavior to the paramagnetic phase. A linear dependence is determined between the surface (and interface) energy and the variation of the number of chemical bonds weighted by the respective bond strength, which can be used to predict the relative formation energy for the surface and interface with various chemical terminations. Finally, the critical stresses of both intraprecipitate and interfacial fractures due to a tensile loading are estimated via the universal binding energy relation (UBER) model, parametrized on the DFT data. The validity of this model is verified in the case of intraprecipitate fracture, against results from DFT tensile test simulations. In agreement with experimental evidences, we predict a much stronger tendency for an interfacial fracture for this carbide. In addition, the calculated interfacial critical stresses are fully compatible with available experimental data in steels, where the interfacial carbide-matrix fracture is only observed at incoherent interfaces.

DOI: 10.1103/PhysRevMaterials.2.023605

I. INTRODUCTION

The presence of precipitates, for instance carbides, in metal alloys has a strong impact on the mechanical properties of the materials [1–3]. So far, several experiments have shown an interfacial decohesion between second-phase particles and the metallic lattice in, for example, steels [4–7] and nickel-based alloys [8]. Also, some other precipitates show an intraprecipitate fracture [9–11].

The occurrence of either an interfacial or an intraprecipitate decohesion mainly depends on the characteristics of the precipitates, such as chemical configuration, the precipitate and the interfacial structure, and the size of the precipitates [12]. For example, it is known by experiments that an interfacial fracture occurs for the case of the $M_{23}C_6$ in both ferritic and austenitic steels, whereas an intraprecipitate fracture tends to occur for the M_3C in steels [13]. Also, Gammage *et al.* [14] have observed that inhomogeneity in the precipitate distributions causes local concentration of stress which is certainly responsible for interfacial heterogeneous fracture initiation.

Understanding the mechanisms of precipitate-matrix decohesion is necessary to improve the prediction of creep and ductile damage evolution, to obtain a more accurate estimate of material lifetimes. Previously, to simulate and interpret the interfacial decohesion, two models have been developed. The first one is the Raj model [15], which is a model that explains the interfacial decohesion by vacancy agglomeration. However, Lim *et al.* [16] has shown that the Raj model does not correctly predict the dependence of properties of interfacial decohesion as a function of temperature and applied stress. The second model [17] considers rather the microcrack initiation at the interface assuming a brittle fracture. Then, the Dyson law [18], which takes into account the interfacial fracture, could be used to simulate the damage at a larger spatial scale. Previously, this law was frequently applied to obtain microcrack initiation from reversed identification [19] or experimental measurements [17]. Based on an accurate prediction of microcrack initiation, the Dyson law is expected to correctly predict the damage evolution [17]. The objective of this paper is to predict the interfacial fracture energy and the critical stress, which is the first step toward the prediction of microcrack initiation.

We aim at predicting these interfacial properties based on first-principles calculations and the universal binding energy relation (UBER) model [20], without the use of experimental or fitting parameters. The UBER model [21] is originally based on an exponential decay of electronic density as a function of the distance between two atomic planes in a pure metal system. Previous authors have used the original formulation of this model to fit tensile curves obtained by atomistic simulations of tensile tests [22–31]. These atomistic simulations may be very computationally demanding if performed at a first-principles

2475-9953/2018/2(2)/023605(13)

level and if complex systems are considered. Recently, Enrique *et al.* [32] have shown a good agreement between results from the UBER model and from density functional theory (DFT) tensile test simulations in bulk Al.

The present study focuses on coherent interfaces between a fcc metallic matrix (Fe, Ni) and a representative carbide in steels and in Ni alloys, $M_{23}C_6$. In most cases, $M_{23}C_6$ carbide contains chromium as the major metal component [2]. We therefore consider here $Cr_{23}C_6$ carbide as a first representation of $M_{23}C_6$. We also aim at investigating the effects of interfacial structural and chemical configuration, and of the magnetic ordering and disordering of the metallic lattice. In particular, the paramagnetic fcc Fe is represented by a magnetic special quasirandom (MSQS) configuration. Special attention is paid to the correlation between electronic, magnetic, energetic, elastic, and fracture properties.

II. METHODOLOGY

A. Density functional theory calculations

1. Computational methods

DFT [33,34] calculations are performed to determine structural, elastic, and energetic properties of the metal and the carbide bulk, surfaces, and interfaces.

The Vienna *ab initio* Simulation Package (VASP) [35,36] code is used. All the calculations are spin polarized within the collinear magnetism scheme and employ the generalized gradient approximation (GGA) [37] with the Perdew, Burke, Ernzerhof (PBE) scheme [38]. The interaction between ions and electrons is described by projector augmented wave (PAW) potentials. As valence electrons, $3d$ and $4s$ electrons are considered for iron, nickel, and chromium, and $2s$ and $2p$ electrons are considered for carbon. We verified that the properties of interest are sufficiently converged by adopting plane-wave basis sets with an energy cutoff of 500 eV. For the Brillouin-zone sampling, the Methfessel–Paxton [39] smearing function of a 0.3 eV width is used. Concerning the K points, the Monkhorst–Pack scheme [40] is used and the K-point grid is $12 \times 12 \times 12$ in the fcc unit cell (29 atoms) of the carbide and $16 \times 16 \times 16$ for the cubic unit cell (four atoms) of a fcc metallic (Fe or Ni) system. We used a cutoff condition of 10^{-6} eV for the electronic convergency loops and of 0.02 eV/Å on the residual forces for the structural optimizations. Three-dimensional periodic boundary conditions are applied. We performed constant-volume calculations unless otherwise mentioned.

2. Surface-formation energy

The slab method allows us to calculate the surface energy with periodic boundary conditions. A supercell then contains two free surfaces and at least 10Å of vacuum. For a one-element system, the surface-formation energy can be obtained as

$$E_{\mathrm{surf}} = \frac{E_{\mathrm{slab}} - E_0}{2A}, \tag{1}$$

where E_{slab} is the total energy of the slab with two free surfaces, E_0 is the total energy of the reference bulk system containing the same number of atoms as in the slab, and A is the surface area. For a compound; for instance, carbide, Eq. (1) enables us to calculate the formation energy of a given surface if the slab remains stoichiometric. However, a $Cr_{23}C_6$ slab showing two identical surfaces is generally nonstoichiometric. For this case, we adopted the approach described by Rapcewicz *et al.* [41] based on a chemical-potential analysis. Other authors also applied this method to determine surface and interface energies [42–44]. Within this approach, equilibrium between the bulk and the surface is assumed. A generalized expression for the surface energy can be written as

$$E_{\mathrm{surf}} = \frac{1}{2A}\left(E_{\mathrm{slab}} - \sum_{i=0}^{n} N_i \mu_i\right), \tag{2}$$

where A is the surface area, E_{slab} is the total energy of the system including two free surfaces, N_i is number of atoms of species i, μ_i is the corresponding chemical potential of species i in the system, and n is the number of species. The chemical potential of a unit formula of $Cr_{23}C_6$ can be written as

$$\mu_{\mathrm{Cr_{23}C_6}} = N_{\mathrm{Cr}}\mu_{\mathrm{Cr}} + N_{\mathrm{C}}\mu_{\mathrm{C}} = N_{\mathrm{Cr}}\mu_{\mathrm{Cr}}^{P} + N_{\mathrm{C}}\mu_{C}^{P} + \Delta H_0^F, \tag{3}$$

with ΔH_0^F being the carbide enthalpy of formation of the stoichiometric carbide, and μ_i^P being the chemical potential of species i in the respective reference pure bulk system. Because the compound is thermodynamically stable, the chemical potential of each species must be lower than the corresponding chemical potential of the pure systems; that is, graphite for C and bcc Cr:

$$\mu_{\mathrm{Cr}} \leqslant \mu_{\mathrm{Cr}}^{P} \text{ and } \mu_{\mathrm{C}} \leqslant \mu_{\mathrm{C}}^{P}. \tag{4}$$

Using Eq. (3), we can rewrite Eq. (2), and the resulting surface energy is a function of only one variable, the chemical potential of carbon:

$$E_{\mathrm{surf}} = \frac{1}{2A}\left[E_{\mathrm{slab}} - \mu_{\mathrm{Cr_{23}C_6}}\left(N^{\mathrm{Cr_{23}C_6}} + \frac{N_{\mathrm{Cr}}^{\mathrm{ex}}}{23}\right) + 6\mu_{\mathrm{C}}\left(\frac{N_{\mathrm{C}}^{\mathrm{ex}}}{6} - \frac{N_{\mathrm{Cr}}^{\mathrm{ex}}}{23}\right)\right], \tag{5}$$

with N_i^{ex} being the atom number of species i in excess (with respect to the stoichiometric ratio) and $N^{\mathrm{Cr_{23}C_6}}$ being the number of unit formulas of $Cr_{23}C_6$. Using Eq. (4), the range of the carbon chemical potential is

$$\frac{\Delta H_0^F}{N_C} \leqslant \mu_C - \mu_C^P \leqslant 0.$$

It is possible to give a more precise estimate of the surface energy by further limiting the variation of the carbon chemical potential with the consideration of the next carbide in the phase diagram, which is Cr_7C_3 (Fig. 1). Therefore the new range for the chemical potential becomes

$$\frac{\Delta H_0^F(\mathrm{Cr_{23}C_6})}{N_{\mathrm{C}}} \leqslant \mu_{\mathrm{C}} - \mu_{\mathrm{C}}^{P} \leqslant \frac{\Delta H_0^F(\mathrm{Cr_7C_3})}{N_{\mathrm{C}}}. \tag{6}$$

3. Interface-formation energy

Supercells are used to represent metal-carbide interfaces. To determine the interface-formation energy with a given carbide termination, two identical interfaces are included in each

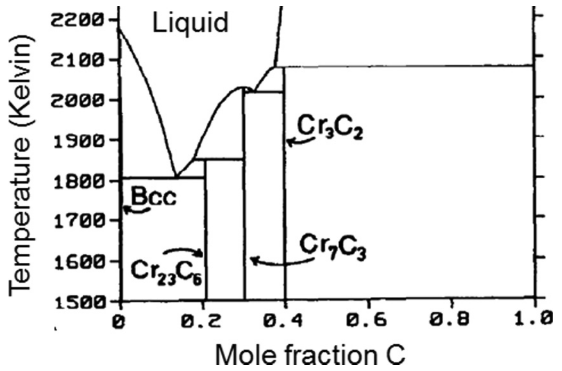

FIG. 1. Partial chromium-carbon phase diagram from Andersson [45].

supercell. If the carbide subsystem remains stoichiometric, the interface energy can be written as

$$E_{\text{inter}} = \frac{E_{\text{total}}^{\text{inter}} - E_{\text{carbide}} - E_{\text{matrix}}}{2A}, \tag{7}$$

with $E_{\text{total}}^{\text{inter}}$ being the total energy of the supercell including two identical interfaces, E_{carbide} being the total energy of the carbide bulk containing the same number of Cr and C atoms as in the interface system, and E_{matrix} being the total energy of the metal (Fe or Ni) bulk system.

Generally, a deviation from stoichiometry occurs if two identical interfaces are created. In the present study, interdiffusion and interface roughness are neglected. Then, assumptions similar to those for the nonstoichiometric carbide surfaces can be adopted.

The resulting interface energy can be written as

$$E_{\text{inter}} = \frac{1}{2A}\left[E_{\text{total}}^{\text{inter}} - N_{\text{Fe}}\mu_{\text{Fe}} - \mu_{\text{Cr}_{23}\text{C}_6}\left(N^{\text{Cr}_{23}\text{C}_6} + \frac{N_{\text{Cr}}^{\text{ex}}}{23}\right) + 6\mu_{\text{C}}\left(\frac{N_{\text{C}}^{\text{ex}}}{6} - \frac{N_{\text{Cr}}^{\text{ex}}}{23}\right)\right]. \tag{8}$$

In this equation, the interface energy is given as a function of the carbon chemical potential in the Cr_{23}C_6. The same notation as for Eq. (5) is adopted.

4. *Fracture energy and Griffith energy*

As a first approximation, the fracture energy is assumed to be the Griffith energy. The Griffith energy is defined as the energy required for a perfect brittle fracture:

$$\gamma_{\text{Griffith}} = \gamma_{\text{Surf}_1} + \gamma_{\text{Surf}_2} - \gamma_{\text{inter}}, \tag{9}$$

where γ_{Surf_i} is the surface-formation energy of system i and γ_{inter} is the interface energy. Therefore, the Griffith energy γ_{Griffith} is the energy difference between a system containing two free surfaces and a system with the initial interface. Please note that, were the number of atoms of each species identical in the interface and the surface systems, the Griffith energy would become independent of the chemical potentials:

$$E_{\text{Griffith}} = E_{\text{slab}}^{\text{carbide}} + E_{\text{slab}}^{\text{metal}} - E_{\text{total}}^{\text{inter}}. \tag{10}$$

B. Universal binding energy relation (UBER) model for critical-stress calculations

Rice and Wang [46] developed an expression for the critical stress of fracture based on the original UBER model [20]. The critical stress is written as a function of the interfacial fracture energy (γ_{fract}), an interfacial thickness (d_0), and an effective Young's modulus associated with the interfacial region (Y^{inter}):

$$\sigma_c = \frac{1}{e}\sqrt{\frac{\gamma_{\text{fract}} Y^{\text{inter}}}{d_0}}. \tag{11}$$

Note that this expression enables a direct estimate of the critical stress, while if applying the original formulation of Rose *et al.* [20], several total-energy calculations with distinct interfacial separations are required to obtain the energy and the stress curves. In this study, all the parameters for this Rice and Wang UBER model are obtained via DFT calculations.

It is worth mentioning that, within this model, the interface is considered as a three-dimensional object, and there is no a unique way to determine the called interfacial thickness. For instance, one plausible criterion is to consider as the interfacial region where relevant atomistic properties such as the interatomic distances and the local magnetic moments differ significantly from the corresponding values in the bulk. This criterion clearly implies certain arbitrariness. Another possibility is to take the region that includes all the first nearest neighbors ($1nn$) of all the atoms of the first interfacial layer. For simplicity, we adopted the latter criterion in this study. Some discussion of the dependence of the critical stress on the interfacial thickness is given below.

III. RESULTS AND DISCUSSIONS

In this section we determine and analyze the fracture properties of the Cr_{23}C_6 carbide and of the carbide-metal interfaces based on atomic-scale properties obtained by DFT calculations. We pay particular attention to the correlation between the electronic, magnetic, energetic, elastic, and fracture properties. We start with the relevant bulk and surface properties of fcc Fe and Ni as functions of the magnetic state. Then, the bulk and surface structures of the carbide are described. Finally, we discuss the metal-carbide interfacial properties, the fracture energy, and the critical stress under a uniaxial tensile strain.

A. Bulk and surface properties of fcc Fe and Ni

Various properties of fcc iron and nickel are studied as reference data for the study of surfaces and interfaces. The fcc iron and nickel are chosen as first representations of the austenitic steels and Ni-based alloys, respectively, where the $M_{23}\text{C}_6$ carbides are frequently observed.

Calculated lattice parameters, elastic moduli, and local magnetic moments are shown in Table I for Fe and Ni. The elastic moduli are determined from the DFT calculated elastic constants. For the ordered magnetic states, many DFT data are available in literature [47–50]. All the present values for Fe are in good agreement with the previous DFT results, except for the bulk modulus of the antiferromagnetic (AF) state, for which we predict a value 25% larger. Note that the magnetic

TABLE I. Bulk properties of Fe and Ni at various magnetic states: the antiferromagnetic (AF), the ferromagnetic (FM), the nonmagnetic (NM), double-layer antiferromagnetic (AFD), and the paramagnetic (PM) state, where a_0 denotes the lattice constant, ΔE is the relative energy with respect to the reference states (the bcc-FM state for iron and fcc-FM state for Ni), M is the local magnetic-moment magnitude, and Y is the (100) Young's modulus. For the AF and AFD states, it is the value of the direction of the magnetic stacking, Y^2 is the Young's modulus along one of the perpendicular directions, B is the bulk modulus, and G is the shear modulus (perpendicular to the magnetic stacking axis for AF and AFD Fe). The properties for two FCT phases are also shown for comparison. Values from previous studies are given in parentheses.

Metal	a_0 (Å)	c/a	ΔE (eV)	M (μ_B)	Y (GPa)	Y^2 (GPa)	B (GPa)	G (GPa)
Fe bcc FM	2.831	1	0	2.2	180		200	103
Guo *et al.* [53]	(2.84)			(2.2)	(185)		(186)	(99)
Fe fcc NM	3.446	1	0.16	0	285		282	222
Herper *et al.* [47]				(0)			(290)	
Fe fcc AF	3.487	1	0.12	1.3	165	215	240	207
Herper *et al.* [47]				(1.3)			(188)	
Fe fcc FM	3.636	1	0.15	2.6	−365		180	−106
Guo *et al.* [53]	(3.63)			2.55	(−270)		(182)	
Fe fcc AFD	3.537	1	0.10	1.9	−12	−40		
Klaver *et al.* [54]	(3.527)			(1.8)	(32)	(10)		
Fe fcc PM	3.487	1	0.14	1.6	188		130	230
Zhang *et al.* [55]	(3.506)			(1.42)			(131)	(213)
Harste *et al.* [56]					(230)			
Fe fct AF	3.433	1.051	0.10	1.47	218	176		
Klaver *et al.* [54]	(3.423)	(1.069)		(1.5)	(213)	(154)		
Fe fct AFD	3.449	1.095	0.081	2.05	169	1		
Klaver *et al.* [54]	(3.447)	(1.088)		(1.99)	(170)	(2)		
Ni fcc NM	3.512	1	0.05	0	128		197	123
Guo *et al.*	(3.51)			(0)	(129)		(207)	(40)
Ni fcc FM	3.519	1	0	0.65	156		199	129
Shang *et al.* [48]	(3.521)				(157)		(198)	
Experimental	(3.517 [57])			(0.6 [49])	(138 [58])		(188 [50])	

ground state of fcc Fe is a spin spiral. But, within a collinear-magnetism approximation, the double-layer antiferromagnetic (AFD) is the lowest-energy magnetic state. The antiferromagnetic (AF) is also a low-energy local minimum. Concerning the elastic moduli, at least one of the Young moduli for the AFD and the fcc ferromagnetic high-spin (FM) iron is negative or almost zero. These states are expected to be mechanically unstable and are therefore not considered in the following. Both austenitic (Fe-Ni-Cr) alloys and the fcc iron exhibit a paramagnetism (PM) for a wide range of temperatures of technological interests. To mimic the PM state of fcc iron, we adopted a magnetic quasirandom structure (MSQS) using a supercell containing 108 atoms. A MSQS state consists of a state with zero total magnetization and a minimum of magnetic short-range order [51,52]. All the atoms are fixed on their positions of a perfect fcc lattice; that is, forces caused by the inequivalence of local magnetic environments are ignored, as assumed in Ref. [51]. It is interesting to note that it has also a low energy; for instance, compared with the FM and the NM (nonmagnetic) states. Concerning fcc Ni, the calculated properties for the magnetic ground state, the ferromagnetic, and the NM are in good agreement with available experimental and DFT data.

It is worth mentioning that the calculated elastic moduli for the PM Fe are closer to those of the AF Fe compared with those of the NM Fe. As known experimentally along the thermal expansion, the elastic moduli strongly depend on the atomic volume. On the other side, they are also very sensitive to the change of the magnitude of local Fe moments, and the latter depend on the atomic volume dictated by the well-known magneto-volume effect. We are therefore interested in determining the Young's modulus as a function of both atomic volume V and local magnetic-moment magnitude M as variables. Based on the data shown in Figs. 2(b) and 2(c), an expression for Y can be proposed as

$$Y = \alpha V + \beta M + \gamma V M + \varepsilon, \tag{12}$$

where the greek letters denote the fitting parameters, with $\alpha = -70.47\ \text{GPa}/\text{Å}^3$, $\beta = -152.94\ \text{GPa}/\mu_B$, $\gamma = 10.98\ \text{GPa}/(\text{Å}^3 \mu_B)$, and $\varepsilon = 1010$ GPa, assuming the AF state of fcc iron. It is worth noting that both α and β are negative. The sign of the former is consistent with the experimentally observed decrease of elastic moduli versus temperature for metals. The magnitude of β is larger than that of α, suggesting a stronger decrease of Y with increasing magnitude of the Fe moment.

For the metallic surfaces, we focus on the (100) orientation (for the AF fcc Fe, it is parallel to the magnetic stacking direction), which allows the formation of the lowest-index coherent interface with the $Cr_{23}C_6$ carbide, also along a (100) direction [2,59]. Indeed, in this case, the misfit between the lattice constant of the carbide and three times the lattice constant of any of the metallic systems is lower than 1.1%,

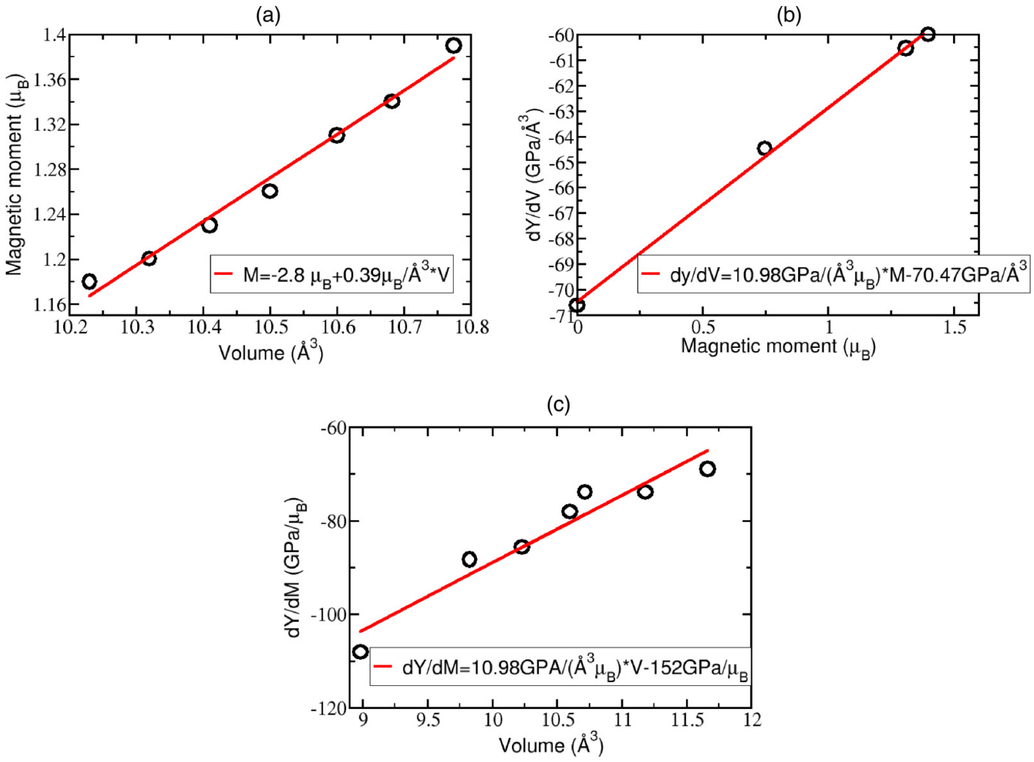

FIG. 2. (a) Variation of magnetic moment as a function of atomic volume. (b) Volume derivative of Young's modulus at fixed magnetic moment. (c) Magnetic-moment derivative of Young's modulus at fixed volume, for fcc AF iron.

which is comparable to the case of coherent precipitate-matrix interfaces in concentrated Fe-Cr alloys, observed experimentally [60]. To investigate properties of the metal surfaces, the slab method is used [Eq. (1)] with 12 atomic layers in the direction perpendicular to the surface, and at least 10 Å of vacuum along the same direction.

For both Fe and Ni, a significant variation of the surface energies is observed depending on the magnetic ordering (Table II). As expected, the presence of magnetism stabilizes the [100] surface. Therefore, the surface energy decreases if the system is magnetic. As in the case of fcc bulk iron, the surface energy of PM iron is estimated by using a slab with a MSQS configuration. To ensure the magnetic disorder at the surface, the slab contains 18 Fe atoms per layer parallel to the surfaces. The relaxed atomic positions of an equivalent slab with an AF ordering are adopted. Again, as in the bulk case, this approximation provides a simplified way to consider the adiabaticity, by assuming that the characteristic time for magnons is much shorter than that for atomic relaxations.

TABLE II. Formation energy of Fe(100) and Ni(100) surfaces for four magnetic states: the FM, NM, AF, and the PM. Some previous experimental [61], and calculated data [62–64] are also given.

	E_{surface} (eV/atom)	E_{surface} (J/m^2)	Previous work (J/m^2)
Fe fcc NM	1.23	3.32	1.95 [61], 2.13 [62]
Fe fcc AF	0.95	2.51	1.95 [61], 2.13 [62]
Fe fcc PM	1.12	2.95	
Ni fcc NM	0.87	2.26	
Ni fcc FM	0.86	2.22	2.16 [63], 2.42 [64]

Within this frame, it is necessary to exclude forces caused by inequivalent local magnetic environments. No further structural optimization is performed. In Fig. 3, bulk-like properties are found at the center of the slab with a relative difference lower than 1%. This indicates a reasonable convergence of the calculated surface energies as a function of the slab thickness. In Fig. 3(b), we also note that a coordination fault induces an increase of magnetism at the surfaces for both paramagnetic (PM) and antiferromagnetic (AF) cases [65].

B. Bulk and surface properties of the $Cr_{23}C_6$ carbide

1. $Cr_{23}C_6$ *bulk*

$M_{23}C_6$ is a representative carbide observed in the austenitic steels [17] in Fe-Cr–based ferritic steels [1], and in Ni-based alloys [8]. In this study, a simple representation of $M_{23}C_6$, $Cr_{23}C_6$, is adopted, because in many cases chromium is the major metal component of this carbide [2]. Previous DFT results [66–68] showed that $Cr_{23}C_6$ has a fcc structure $Fm\bar{3}m$ with a basis of 23 Cr atoms and 6 C atoms at each fcc site. The calculated lattice constant ranges from 10.527 Å to 10.607 Å. The lattice constant found in this work (10.524 Å) is in good agreement with the previous DFT values. On the other hand, the experimental lattice constant for the $M_{23}C_6$ determined at room temperatures is 10.659 Å. The calculated-experimental difference may be mostly due to a difference of chemical composition. Indeed, experimentally, the carbide is not only composed of chromium and carbon.

The Wyckoff atomic positions are computed by Xie *et al.* [69] based on experiments, and these positions are $4a$, $8c$, $32f$, and $48h$ for the chromium atoms and $24e$ for the carbon atoms

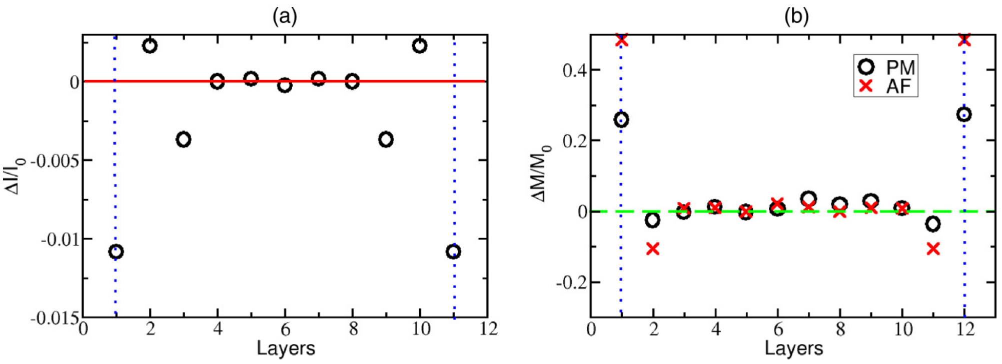

FIG. 3. Relative variation of properties with respect to the bulk values for different layers of the slab with two free surfaces: (a) interlayer distances ($\frac{\Delta I}{I_0}$) in the AF-Fe and (b) local magnetic moments ($\frac{\Delta M}{M_0}$) in the AF and the PM Fe. Surface layers are indicated with vertical dotted lines.

(Table III); that is, there are four symmetrically different types of Cr atoms while all the C atoms are equivalent. Each C atom is located at the so-called squared antiprismatic site, with eight 1*nn* Cr atoms. Table III shows a good agreement between the Wyckoff and the DFT calculated positions. A side view of the atomic structure of the chromium carbide can be seen in Fig. 4(a).

Concerning the magnetic state of the carbide, it is known that Cr atoms tend to display an antiferromagnetic ordering. But in this carbide, a triangular arrangement is found for groups of three Cr atoms, inducing a magnetic frustration. The carbide becomes therefore nonmagnetic. However, it is known that if Fe atoms are included in $M_{23}C_6$, a nonzero magnetization is induced [68].

2. *Carbide surfaces*

As in the case of the metallic surfaces, we only focus on the [100] surface of the carbide in this study. The stacking of atomic layers in the (100) direction is shown in Fig. 4(b). There are five distinct surface layers but eight possible surface terminations accounting for the subsurface layer. To optimize the surface structure, we have calculated and compared the surface energy of all the possible terminations. Slabs composed of at least 16 atomic layers (10.524 Å) and 10 Å of vacuum are used. Note that the slab system becomes nonstoichiometric if creating two identical surfaces. The approach described in Sec. II A 2 is therefore adopted. As shown in Fig. 5, the variation of the surface energies is significant within the total range of the carbon chemical potential [Eqs. (4) with (5)]: $\frac{\Delta H_0^F}{N_C} \leqslant \mu_C - \mu_C^B \leqslant 0$. But it becomes negligible if a reduced range of the chemical potential is considered, accounting for the next carbide in the phase diagram, Cr_7C_3 (see inset in Fig. 5). As a result, a rather precise estimation of the surface energy for each termination can be obtained by using the respective averaged value. The obtained surface energies are given in Table IV. The notation used for the description of carbide terminations is $\alpha(\beta)$ where α is the surface and β is the subsurface layer.

To rationalize the relative stability of the various terminations, the surface energies are plotted as a function of the weighted number of broken bonds (Fig. 6). To calculate the latter, the following expression is used:

$$\Omega_{\text{surf}} = \sum_{i}^{n} N_{bi} Q_i, \tag{13}$$

where N_b is the number of broken bonds due to the surface creation, and Q_i is the off-diagonal elements of the Mulliken population matrix obtained with complementary calculations using the localized basis set of the DFT-SIESTA code [70]. These elements provide the amount of electronic charge accumulation between two neighboring atoms, which is proportional to

TABLE III. Comparison between the experiment-based [69] and the DFT-calculated fractional atomic positions with respect to lattice vectors of a simple-cubic unit cell in $Cr_{23}C_6$ carbide.

Wyckoff positions	Experiment	DFT	Deviation in %
4*a*	0	0	0
8*c*	0.25	0.25	0
8*c*	0.75	0.75	0
32*f*	0.385	0.380	1.3
32*f*	0.615	0.619	0.6
48*h*	0.165	0.169	2.4
48*h*	0.835	0.830	0.6
48*h*	0	0	0
24*e*	0	0	0
24*e*	0.275	0.276	0.3
24*e*	0.725	0.723	0.3

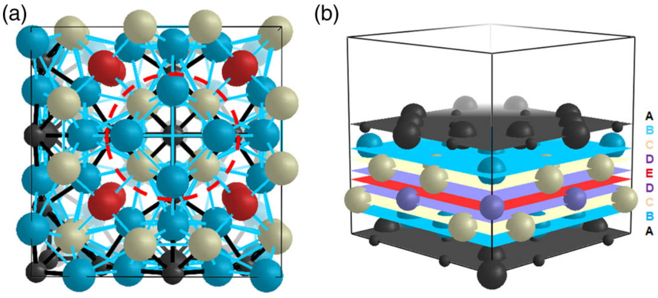

FIG. 4. (a) Cubic unit cell of $Cr_{23}C_6$ carbide where the small spheres are C atoms, and the big spheres of different colors represent the four symmetrically inequivalent types of Cr atoms. A C atom located at a squared antiprismatic site with its eight Cr nearest neighbors is circled in red. (b) Stacking of $Cr_{23}C_6$ in (100) direction, where successive atomic planes are denoted by different colors.

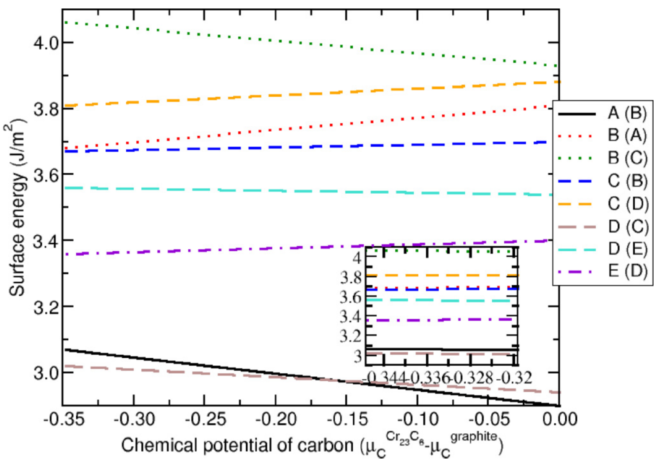

FIG. 5. Surface energy of $Cr_{23}C_6$ in a (100) direction as a function of the chemical potential of carbon. The notation used for the different terminations is $\alpha(\beta)$, where α is the surface and β is the subsurface layer. The inset shows the surface-energy variation in the reduced range of the chemical potential when considering Cr_7C_3 carbide.

the bond strength. Here i denotes the type of the chemical bond (Cr-C or Cr-Cr). We note that only $1nn$ bonds are relevant. The surface energy is reasonably described by a linear function of Ω_{surf} as shown in Fig. 6, which can be written as $\gamma_S = (0.59\ \frac{\mathrm{J}}{\mathrm{m}^2 e^-})\Omega_{\mathrm{surf}} + 0.06\ \mathrm{J/m}^2$. In Table IV, the surface energy and the corresponding number of broken Cr-C and Cr-Cr bonds and the resulting Ω_{surf} are given. As expected, the Cr-C bond strength ($0.19e^-$) is stronger than the Cr-Cr bond strength ($0.12e^-$) due to the covalent character of the former. Therefore, the number of broken Cr-C bonds has a dominant effect on the surface energy. However, there are generally more broken bonds of the Cr-Cr type. Their global effect may be not negligible. It is worth mentioning that such a simple linear relationship is useful for a first prediction of the relative surface energies of distinct terminations for a given surface orientation, providing that there is not an especially strong structural relaxation or reconstruction at the surface.

C. Metal-carbide interfaces

Properties of the metal-carbide interfaces such as the interface structure, the interface and the Griffith energies, and the effective interfacial Young's modulus are discussed in this section. We focus on the coherent (100) interfaces and the fcc Fe and Ni as the metallic matrix.

TABLE IV. Formation energy of the (100) carbide surface, the number of broken Cr-Cr and Cr-C bonds for the different terminations, and Ω_{surf}, the latter which is the resulting total number of broken bonds weighted by the respective bond strength: $0.19e^-$ for Cr-C and $0.12e^-$ for Cr-Cr.

Surface	E_{surface} (J/m^2)	Cr-Cr bonds	Cr-C bonds	Ω_{surf} (e^-)
A (B)	3.05	32	8	5.36
B (A)	3.67	30	12	5.88
B(C)	4.05	31	16	6.76
C (B)	3.68	32	12	5.92
C (D)	3.8	36	12	6.6
D (C)	3.01	30	8	5.12
D (E)	3.56	36	8	5.84
E (D)	3.36	20	16	5.44

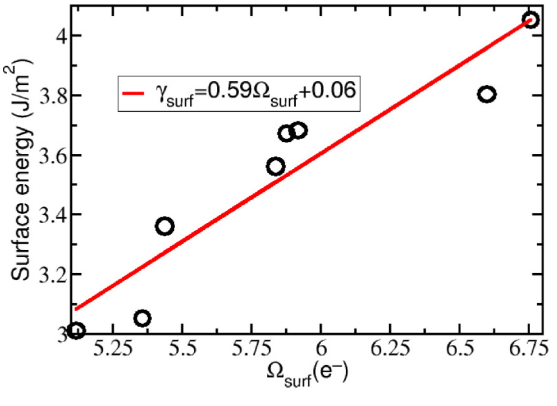

FIG. 6. Surface energy of carbide as a function of weighted number of broken bonds (Ω_{surf}).

1. *Interface structure and energy*

For the construction of the interfaces, it is also necessary to optimize the interface structures in terms of the interface energy. The latter is calculated following the methodology described in Sec. II A 3, similar to the case of carbide surfaces. Supercells containing two identical interfaces each are used for this purpose. The length of the supercells in the direction perpendicular to the interface is around 30 Å, including 12 Å of the carbide and 18 Å of the metal. The supercells contain between 166 and 200 atoms depending on the carbide termination. We have verified that bulk-like properties are found in the middle between the two interfaces. For example, as shown in Fig. 7, a deviation less than 3% is noted for the magnetic-moment magnitudes for the AF and the PM iron matrix and a deviation less than 2% is noted for the interlayer distance for the AF. Besides, at variance with the metallic surfaces, a decrease of the Fe-moment magnitude at the interface is noted following by an increase at the subinterface layer.

The resulting interface layer is the lowest for the A interface, formed with the (100) surface of the metal and the A-terminated (100) carbide surface. In the following, our discussion will mainly focus on this interface. To further optimize the interface structure, we note that, for all eight distinct interfaces, three high-symmetry interfaces can be identified by rigidly shifting the metal and the carbide blocks. To give an illustration, they are schematically represented in Fig. 8 for the interface between an A-terminated carbide surface and a metallic matrix. The configuration of Fig. 8(a) is called hollow configuration where each Cr atom is surrounded by four metallic atoms, while the configuration of Fig. 8(b) is a bridge configuration where a Cr atom is located between two matrix atoms, and Fig. 8(c) shows a top configuration where a surface Cr atom is on top of one matrix atom. In the following, we only consider the hollow configuration because it is the lowest-energy configuration of all the cases.

As for the carbide surfaces, an analysis in terms of the bond strength is also performed for the interfaces. In Table V, Ω_{int} is the weighted number of broken bonds (Cr-C, Cr-Cr, and

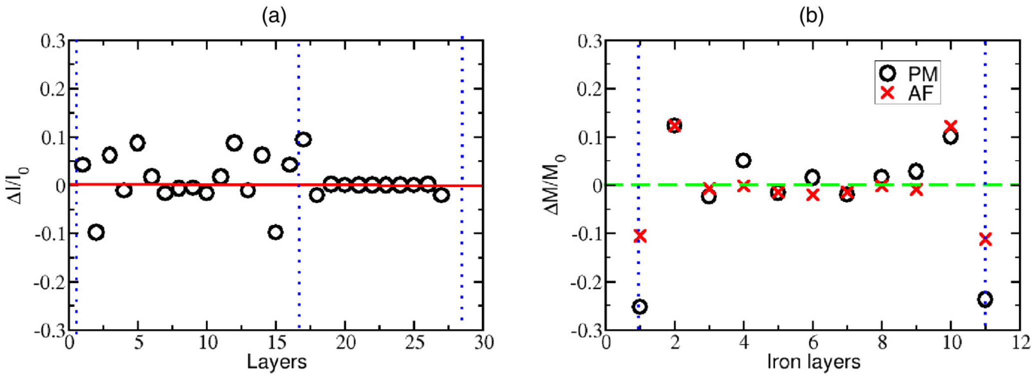

FIG. 7. Relative variation of properties for the interface system with respect to the corresponding bulk values: (a) the interlayer distance ($\frac{\Delta I}{I_0}$) in the AF-Fe case, (b) local Fe magnetic moments ($\frac{\Delta M}{M_0}$) for the case of AF and PM Fe.

Fe-Fe) and of newly established (C-Fe and Cr-Fe) bonds for a Fe-carbide interface:

$$\Omega_{\text{int}} = N^{\text{old}}_{\text{Cr-Cr}} Q_{\text{Cr-Cr}} + N^{\text{old}}_{\text{Cr-C}} Q_{\text{Cr-C}} + N^{\text{old}}_{\text{Fe-Fe}} Q_{\text{Fe-Fe}} - N^{\text{new}}_{\text{Cr-Fe}} Q_{\text{Cr-Fe}} - N^{\text{new}}_{\text{C-Fe}} Q_{\text{C-Fe}}, \tag{14}$$

where N^{old} is the number of broken bonds, N^{new} is the number of new bonds due to the interface-formation, with $Q_{\text{Cr-Cr}} = 0.12e^-$, $Q_{\text{Cr-C}} = 0.19e^-$, $Q_{\text{Fe-Fe}} = 0.11e^-$, $Q_{\text{Cr-Fe}} = 0.10e^-$, and $Q_{\text{C-Fe}} = 0.18e^-$.

Figure 9 shows the interface energies versus Ω_{int}. As for the carbide surfaces, the results show again a rather linear behavior, which can be expressed as $\gamma_{\text{interface}} = (0.33\ \frac{\text{J}}{\text{m}^2 e^-})\Omega_{\text{int}} + 0.13\ \text{J/m}^2$.

2. *Griffith energy*

The Griffith energy is the energy required to break the interface which is also an important parameter controlling mechanical properties. Indeed, the occurrence of interfacial fracture is actually dictated by both the Griffith energy and the critical stress [71]. The Griffith energy is determined by the energy difference between the initial interface (initial state) and the final state exhibiting two noninteracting surfaces [Eq. (9)].

The computed surface, interface, and the Griffith energies are given in Table VI for the case of Fe and Ni with various magnetic configurations and carbide terminations. We note that the variation of the Griffith energy is mainly due to the difference in the metal surface energy. In particular, the emergence of magnetism decreases the Griffith energy caused by the same effect on the metal surface energy. It is interesting to note that the energetic values with the AF-Fe are much closer to those in the PM-Fe case, in spite of the magnetic disordering in the latter. On the other hand, the NM state is clearly not representative of the PM state.

3. *Young's modulus*

To apply the UBER model to predict the critical stress of fracture, another important physical parameter is the Young's modulus associated with the interface. Within this model, an effective constant Young's modulus is attributed to the interface region. To estimate this Young's modulus, a uniform uniaxial stress is assumed through the whole system composed of the metal and the carbide bulk and the (100) interface region in between. Next, the rule of mixture [72] is applied:

$$\varepsilon^{\text{T}} = f^{\text{M}}\varepsilon^{\text{M}} + f^{\text{inter}}\varepsilon^{\text{inter}} + f^{\text{C}}\varepsilon^{\text{C}}, \tag{15}$$

where f^α is the volume fraction of the phase α, ε^α is the average strain in the α phase, with $\alpha = \text{M, C}$ denoting respectively the metal matrix and the carbide. By using Young's law ($\sigma = Y\varepsilon$) in the case of uniaxial stress and for small deformations, Eq. (15) becomes

$$\frac{\sigma}{Y^{\text{T}}} = \frac{f^{\text{M}}\sigma}{Y^{\text{M}}} + \frac{f^{\text{inter}}\sigma}{Y^{\text{inter}}} + \frac{f^{\text{C}}\sigma}{Y^{\text{C}}}. \tag{16}$$

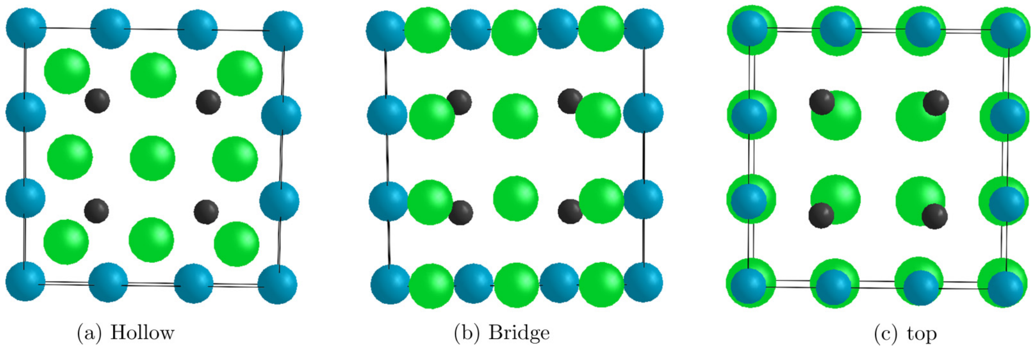
(a) Hollow (b) Bridge (c) top

FIG. 8. The three high-symmetry configurations (top view) of the (100) interface between fcc iron (or nickel) and *A*-terminated $Cr_{23}C_6$ carbide. The blue, black, and green spheres denote respectively Cr, C, and the metal matrix atoms.

TABLE V. Interface energy, number of interfacial Cr-Fe and C-Fe bonds, and Ω_{int}, the weighted number of broken and newly formed bonds at the interface.

Interface	Interface energy $\mathrm{J/m^2}$	Cr-Fe bonds	C-Fe bonds	Ω_{inter} (e^-)
Fe-NM/A(B)	0.800	27	9	1.77
Fe-NM/B(A)	1.94	9	0	5.8
Fe-NM/C(B)	1.074	25	0	3.6
Fe-NM/D(C)	0.836	9	9	2
Fe-NM/E(D)	2.22	9	0	5.2

TABLE VI. Calculated Fe(100), Ni(100), and A-terminated carbide (100) surface energies, the corresponding interface and the Griffith energies, in $\mathrm{J/m^2}$.

Interface	$\gamma_{\mathrm{surf}}^{\mathrm{metal}}$	$\gamma_{\mathrm{surf}}^{\mathrm{carbide}}$	γ_{inter}	$\gamma_{\mathrm{Griffith}}$
Fe-NM/A(B)	3.32	3.05	0.800	5.57
Fe-AF/A(B)	2.51	3.05	0.740	4.82
Fe-PM/A(B)	2.95	3.05	0.910	5.09
Ni-NM/A(B)	2.26	3.05	0.970	4.34
Ni-FM/A(B)	2.22	3.05	1.09	4.18

At equilibrium, by assuming a uniform stress through the system, the equation can be rewritten as

$$\frac{1}{Y^{\mathrm{T}}} = \frac{f^{\mathrm{M}}}{Y^{\mathrm{M}}} + \frac{f^{\mathrm{inter}}}{Y^{\mathrm{inter}}} + \frac{f^{\mathrm{C}}}{Y^{\mathrm{C}}}. \tag{17}$$

Finally the interface Young's modulus results as

$$Y^{\mathrm{inter}} = f^{\mathrm{inter}}\left(\frac{1}{Y^{\mathrm{T}}} - \frac{f^{\mathrm{M}}}{Y^{\mathrm{M}}} - \frac{f^{\mathrm{C}}}{Y^{\mathrm{C}}}\right)^{-1}. \tag{18}$$

To calculate the Young's modulus of the whole system (Y^{T}) containing the interface, DFT simulations of an uniaxial tensile test are performed, limited to small deformations. Tensile strains ε are imposed perpendicularly to the interface, while the stresses in directions parallel to the interface are fully relaxed. Then, the expression by Rasky and Milstein [73] is used to calculate the tensile stress:

$$\sigma = \frac{c}{V}\frac{\partial E}{\partial c} = \frac{1}{Ac_0}\frac{\partial E}{\partial \varepsilon}, \tag{19}$$

where E is the energy of the volume of the system, A is the cross-sectional area, c is the lattice parameter measured along the tensile direction, c_0 is the equilibrium lattice parameter, and ε is the engineering axial strain ($\varepsilon = \frac{c-c_0}{c_0}$). The global Young's modulus Y^{T} can be obtained as the slope of the stress-versus-strain function.

The computed values of the interfacial Young's modulus are listed in Table VII. To analyze the dependence of the Young's modulus on the interfacial structure, we considered three carbide terminations presenting the lowest [E(D)], the highest [C(B)], and an intermediate [A(B)] Griffith energy. We noted a strong variation of the Young's modulus on the interface structure; in particular, it increases with increasing density of the interfacial layer dictated by the distinct carbide terminations. Indeed, the higher-density interface contains overall a larger number of interfacial (Cr-Fe, C-Fe) bonds (see Table V). The interface is therefore more rigid against the applied tensile stress. It is also interesting to note that the interfacial Young's modulus decreases if the metallic Fe lattice is magnetic, where the Young's modulus of the fcc Fe decreases. However, both the metal and the interfacial Young's moduli are rather not sensitive to the disordering of the Fe magnetic moments. For example, their values are similar in the AF- and the PM-iron cases.

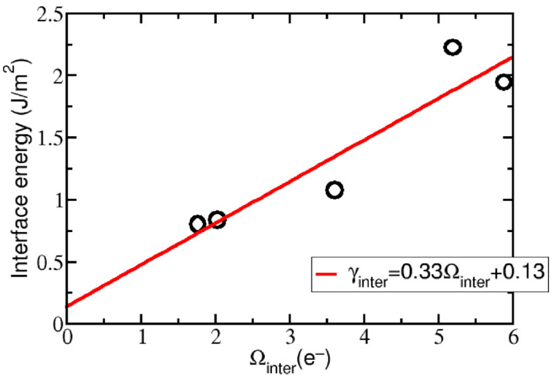

FIG. 9. Interface-formation energy between NM fcc Fe and the carbide as a function of weighted number of broken and newly formed bonds (Ω_{inter}).

To confirm the validity of the rule of mixture for the interfacial Young's modulus, a second method is also used. It consists of a DFT simulation of tensile test, similar to the approach described above, but with strain localized only in the interface region; that is, only atoms near the interface as identified based on the definition of the interfacial thickness are allowed to move. As a result, the interfacial Young's modulus can be directly derived. We have verified that results from this method are in very good agreement with the values from the rule of mixture. For example, for the interface between the A-terminated carbide and the NM-Fe, this method gives an interfacial Young's modulus of 198 GPa whereas the value calculated by rule of mixtures is 202 GPa.

D. Critical stress predicted by universal binding energy relation (UBER) model

The interfacial critical stress is a key parameter for the study of the microcrack initiation and the subsequent cavity growth at

TABLE VII. Young's modulus of metallic matrix, carbide, and interface, and the density of the carbide interfacial layer for each carbide termination.

Interface	Density (atom/Å^2)	Y^{M} (GPa)	Y^{C}(GPa)	Y^{inter}(GPa)
Fe-NM/A(B)	0.1681	285	362	202
Fe-NM/C(B)	0.0748	285	362	148
Fe-NM/E(D)	0.0374	285	362	80
Fe-AF/A(B)	0.1644	165	362	167
Fe-PM/A(B)	0.1644	188	362	100
Ni-NM/A(B)	0.162	119	362	172
Ni-FM/A(B)	0.1615	156	362	162

TABLE VIII. Physical input parameters for the UBER model and the resulting critical stress for interfacial fracture.

Interface	Y^{inter} (GPa)	γ_{Griffith} (J/m^2)	d_0 (Å)	σ_c (GPa)
Fe-NM/A(B)	202	5.57	4.89	20
Fe-NM/C(B)	148	6.14	3.68	18
Fe-NM/E(D)	128	4.37	4.2	13.3
Fe-AF/A(B)	167	4.72	4.62	14.2
Fe-PM/A(B)	100	5.09	4.62	12.3
Ni-NM/A(B)	170	4.24	4.35	14.97
Ni-FM/A(B)	162	4.18	4.42	14.3

the interface. At variance with previous works, we estimate the critical stress for a complex metal-carbide interface by using the UBER model, fully parametrized by DFT data.

The critical stress for interfacial fracture is computed for seven distinct interfaces via the UBER model. The resulting values are given in Table VIII. A dominant dependence of the stress is found on the interfacial Young's modulus, which is itself a function of the interfacial structure, chemical composition, and magnetic state, as discussed above. Please note that the interfacial thickness is the most empirical input parameter for the UBER model. As discussed in Sec. II B, if the other criterion for the interface thickness is considered, its value becomes about two times larger, with a consequent change of the interfacial Young's modulus. However, the critical stress always remains the same order of magnitude. For example, the A-carbide/AF-Fe interface has 11 GPa using the present criterion but 14 GPa using the other criterion. None of the conclusions of this work is changed due to the choice criterion of the thickness.

It is known that fcc iron is generally paramagnetic; however, it is interesting to mention that the interfacial critical stress found with the PM-Fe matrix is much closer to that with the AF-Fe matrix (relative to the NM-Fe matrix), which is also the case for the Griffith energy and the Young's modulus. We therefore suggest that considering the AF iron to represent the PM fcc iron could be an acceptable first approximation for the prediction of the interfacial fracture behavior. Calculations with the former magnetic phase are definitely less demanding computationally.

For interfaces between the carbide and both the Fe and the Ni lattices, the critical stresses obtained are all much (about two times) smaller than the intraprecipitate critical stress for the carbide (Fig. 10), the latter being above 35 GPa. Details of the calculation of the latter is given in Sec. III E. We have also performed additional calculations to determine the critical stress of interfacial fracture between the carbide (with the same A termination) and the bcc FM iron. The value obtained of 19 GPa by the UBER model (with parameters $d_0 = 4.05$Å, $Y^{\text{inter}} = 300$ GPa, and $\gamma_{\text{fract}} = 3.64$ J/m^2) is also significantly smaller than the critical stress of intraprecipitate fracture. These predictions are in excellent agreement with experimental evidence showing interfacial rather than intraprecipitate decohesion for the $M_{23}C_6$ carbides in both austenitic and ferritic steels and in Ni alloys [1,8,17]. A smaller interfacial critical stress compared with the intracarbide stress can be qualitatively explained by the difference between the weighted number of interfacial bonds and the weighted number of interlayer bonds in the carbide. The latter is actually identical to the Ω_{surf} (Sec. III B 2), while the former can be calculated as a function of $Q_{\text{Fe-Cr}}$ and $Q_{\text{Fe-C}}$ as

$$\Omega_{\text{decohesion}} = N_{\text{Fe-C}} Q_{\text{Fe-C}} + N_{\text{Fe-Cr}} Q_{\text{Fe-Cr}}. \quad (20)$$

The resulting number of the intracarbide bonds are all larger than the number of interfacial bonds. For instance, for the A-carbide/metal interface, 27 Fe-Cr bonds and 9 Fe-C bonds formed. And the value of $\Omega_{\text{decohesion}}$ is $4.26e^-$, which is indeed lower than the value of Ω_{surf} (ranging from $5.12e^-$ to $6.36e^-$).

Finally, experimentally, only decohesion of incoherent but not coherent interfaces are observed [17,74] for these carbides in steels and in Ni-based alloys. To reproduce the experimental data, crystalline finite-elements calculations were carried out by Huang [75], who estimated a critical stress of around 5 GPa for austenitic steels. Our higher critical stresses calculated for the coherent interfaces are therefore consistent with these findings. For a quantitative experimental-modelling comparison, further studies, beyond the scope of this paper, should be performed considering the effects of incoherency, of solute segregation, and of biaxial loading.

E. Validation of universal binding energy relation (UBER) model for carbide

To the best of our knowledge, no previous studies has applied the UBER model, fully parametrized on DFT results, to predict the critical stress of complex interfaces. Previous authors have rather used the original formulation of this model to fit the tensile curves obtained by atomistic simulations of tensile tests [22]. To give a first validation of the UBER model, we estimated the critical stress of the $Cr_{23}C_6$ carbide due to tensile strain along a (100) direction with two methods: The first method consists of a homothetic strain with optimization of atomic positions and relaxation of stress perpendicular to the tensile axis [76]. The stress is calculated from the total energy of the system by using Eq. (19). The second method consists of a series of rigid separations of the carbide into two blocks. Similar atomic and stress relaxations as for the first method are applied, but keeping atoms in the foremost four layers of the fracture plane fixed for a given separation. To choose the fracture plane within the carbide, the variation of interlayer distances under the homothetic strain is analyzed. The distance between the consecutive B and C layers is found to be the largest, the fracture plane is therefore set between these two layers for the second method. With the second method, we consider the metal and the carbide bulk under an elastic strain. To obtain the local strain energy and the local stress around the interface, an elasticity correction is used:

$$E_{\text{inter}} = E_{\text{total}} - E_{\text{metal}} - E_{\text{carbide}}, \quad (21)$$

where E_{total} is the total energy of the whole system, E_{metal} and E_{carbide} are the elastic energy for the metal and the carbide, respectively. The elastic energy is given by

$$E_i = \frac{1}{2} Y_i h_i \varepsilon_i^2, \quad (22)$$

where Y_i is the Young's modulus of the i subsystem, h_i, the subsystem dimension parallel to the tensile axis, and ε is the

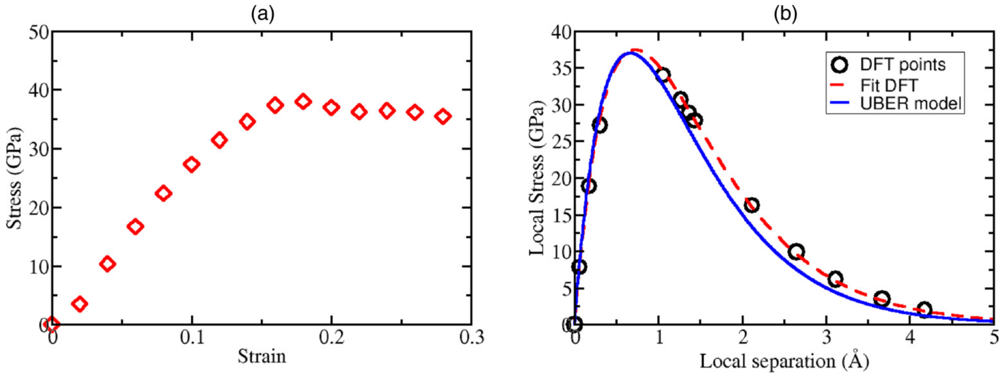

FIG. 10. Comparison between stress caused by uniaxial strain applied to the carbide based on three methods: (1) DFT simulation of homothetic deformation [panel (a)], and (2) DFT simulation with a rigid separation of the carbide, and (3) the UBER model [panel (b)].

strain of *i* subsystem. After subtracting the bulk elastic energy, the interfacial stress can be derived from the local energy versus separation curve as shown in Fig. 10(b).

To apply the UBER model, the parameters used are the Griffith energy between the *B* and *C* terminations (7.73 J/m^2), the Young's modulus of the carbide (362 GPa), and the thickness including the first neighbors (2.5 Å) of atoms at the *B* and the *C* layers

As shown in Fig. 10, a very good agreement is found between the critical stress obtained from the two methods and that predicted by the UBER model, supporting the validity of the UBER model for the present predictions concerning the metal-$Cr_{23}C_6$ interfaces.

IV. CONCLUSIONS

By means of density functional theory calculations, we investigated various electronic, magnetic, structural, and energetic properties, dictating interfacial and intraprecipitate fracture for the $Cr_{23}C_6$ carbide in a Fe or Ni matrix. This carbide is taken as a first representation of $M_{23}C_6$, which is frequently observed in steels and in Ni-based alloys. At variance with previous studies dealing with interfaces and grain boundaries, we have applied the UBER model, fully parametrized on the obtained DFT results, to predict the critical stress for fracture under a uniaxial tensile strain. To the best of our knowledge, such an approach has never been applied to complex interfaces so far.

To estimate the Griffith energy, the surface and interface structures of the carbide are optimized by determining the corresponding formation energies with various carbide terminations. Both stoichiometric and nonstoichiometric structures are considered. For the latter, an analysis based on chemical potentials of the components is performed. A linear relationship is obtained between the surface (interface) energy and the number of broken (broken and newly established) chemical bonds weighted by the respective bond strength, this simple linear law could be used to predict the relative formation energy between various terminations of the surface or interface of any orientation.

All of the relevant interfacial properties (i.e., the formation and Griffith energies and the effective Young's modulus) are analyzed as functions of the magnetic state of the metal lattice. A magnetic special quasirandom configuration in fcc iron is also considered as a first approximation of the paramagnetic phase. Interestingly, a simpler antiferromagnetic phase is found to exhibit similar interfacial properties to the paramagnetic phase. At variance, the nonmagnetic state is not a good representation of the PM state of fcc iron. In particular, the Young's modulus appears to be more sensitive to the variation of the magnitude of the Fe local magnetic moments rather than the ordering of the moments directions.

Finally, the critical stresses of both intraprecipitate and interfacial fracture due to a uniaxial tensile strain are estimated via the UBER model. The validity of this model is verified in the case of intraprecipitate fracture, by means of DFT tensile-test simulations. In agreement with experimental evidence, we predict a much stronger tendency for an interfacial fracture than for an intraprecipitate fracture for this carbide, suggesting that the former may be the cause of the microcrack initiation during, for example, a ductile or a creep damage. In addition, the calculated interfacial critical stresses are fully compatible with available experimental data in austenitic steels, where the interfacial carbide-matrix fracture is only observed at incoherent interfaces.

ACKNOWLEDGMENTS

The DFT calculations were made by using resources from DARI-GENCI under the A0030906020 project, and by using the CINECA-MARCONI supercomputer within the SISTEEL project in the framework of Eurofusion IREMEV programme.

---

[1] J. A. Francis, W. Mazur, and H. K. D. H. Bhadeshia, Mater. Sci. Technol. **22**, 1387 (2006).
[2] T. Sourmail, Mater. Sci. Technol. **17**, 1 (2001).
[3] N. Lopez, M. Cid, and M. Puiggali, Corros. Sci. **41**, 1615 (1999).
[4] A. S. Argon, J. Im, and R. Safoglu, Metall. Trans. A **6**, 825 (1975).
[5] A. S. Argon and J. Im, Metall. Trans. A **6**, 839 (1975).
[6] S. Goods and L. Brown, Acta. Metall. **27**, 1 (1979).

[7] J. Fischer and J. Gurland, Metal Sci. J. **6**, 211 (1981).
[8] G. Young, T. Capobianco, M. Penik, B. Morris, and J. McGee, Weld. J. (Miami, FL, US) **87**, 31s (2008).
[9] L. Babout, E. Maire, and R. Fougres, Acta Mater. **52**, 2475 (2004).
[10] S. Deyber, F. Alexandre, J. Vaissaud, and A. Pineau, in *Superalloys 718, 625, 706 and Derivatives*, edited by E. Loria (TMS, Pittsburgh, 2005), p. 14.
[11] M. N. Shabrov, E. Sylven, S. Kim, and D. H. Sherman, Metall. Mater. Trans. A **35**, 1745 (2004).
[12] A. Asserin-Lebert, J. Besson, and A. Gourgues, Mater. Sci. Eng., A **395**, 186 (2005).
[13] T. Lindley, G. Oates, and C. Richards, Acta. Metall. **18**, 1127 (1970).
[14] J. Gammage, D. Wilkinson, Y. Brechet, and D. Embury, Acta Mater. **52**, 5255 (2004).
[15] R. Raj, Acta. Metall. **26**, 995 (1978).
[16] R. Lim, Numerical and experimental study of creep of Grade 91 steel at high temperature, Ph.D. thesis, Ecole Nationale Suprieure des Mines de Paris, 2011.
[17] Y. Cui, M. Sauzay, C. Caes, P. Bonnaillie, and B. Arnal, Procedia Mater. Sci. **3**, 122 (2014).
[18] B. Dyson, Scr. Metall. **17**, 31 (1983).
[19] H. Riedel, Fracture mechanisms, *Materials Science and Technology* (Wiley-VCH Verlag GmbH and Co. KGaA, Weinheim, Germany, 2006), pp. 1–150.
[20] J. H. Rose, J. Ferrante, and J. R. Smith, Phys. Rev. Lett. **47**, 675 (1981).
[21] A. Banerjea and J. R. Smith, Phys. Rev. B **37**, 6632 (1988).
[22] P. A. Olsson, M. Mrovec, and M. Kroon, Acta Mater. **118**, 362 (2016).
[23] A. M. Tahir, R. Janisch, and A. Hartmaier, Modell. Simul. Mater. Sci. Eng. **21**, 075005 (2013).
[24] N. J. Mosey and E. A. Carter, J. Mech. Phys. Solids **57**, 287 (2009).
[25] A. Srirangarajan, A. Datta, A. N. Gandi, U. Ramamurty, and U. V. Waghmare, J. Phys.: Condens. Matter **26**, 055006 (2014).
[26] R. A. Enrique and A. V. der Ven, J. Appl. Phys. **116**, 113504 (2014).
[27] R. Janisch, N. Ahmed, and A. Hartmaier, Phys. Rev. B **81**, 184108 (2010).
[28] R. Yang S. Tanaka, and M. Kohyama, Philos. Mag. **85**, 2961 (2005).
[29] M. Forti, P. Alonso, P. Gargano, and G. Rubiolo, Procedia Mater. Sci. **8**, 1066 (2015).
[30] S. V. Dmitriev, N. Yoshikawa, M. Kohyama, S. Tanaka, R. Yang, Y. Tanaka, and Y. Kagawa, Comput. Mater. Sci. **36**, 281 (2006).
[31] S. Tanaka, R. Yang, and M. Kohyama, Philos. Mag. **86**, 5123 (2006).
[32] R. A. Enrique and A. V. der Ven, J. Mech. Phys. Solids **107**, 494 (2017).
[33] P. Hohenberg and W. Kohn, Phys. Rev. **136**, B864 (1964).
[34] W. Kohn and L. J. Sham, Phys. Rev. **140**, A1133 (1965).
[35] G. Kresse and J. Furthmüller, Phys. Rev. B **54**, 11169 (1996).
[36] G. Kresse and J. Hafner, Phys. Rev. B **47**, 558 (1993).
[37] J. P. Perdew and Y. Wang, Phys. Rev. B **45**, 13244 (1992).
[38] J. P. Perdew, K. Burke, and M. Ernzerhof, Phys. Rev. Lett. **77**, 3865 (1996).
[39] M. Methfessel and A. T. Paxton, Phys. Rev. B **40**, 3616 (1989).
[40] H. J. Monkhorst and J. D. Pack, Phys. Rev. B **13**, 5188 (1976).
[41] K. Rapcewicz, B. Chen, B. Yakobson, and J. Bernholc, Phys. Rev. B **57**, 7281 (1998).
[42] D. J. Siegel, L. G. Hector, and J. B. Adams, Surf. Sci. **498**, 321 (2002).
[43] A. Dannenberg, M. E. Gruner, A. Hucht, and P. Entel, Phys. Rev. B **80**, 245438 (2009).
[44] E. K. K. Abavare, J.-I. Iwata, A. Yaya, and A. Oshiyama, Phys. Status Solidi B **251**, 1408 (2014).
[45] J.-O. Andersson, CALPHAD: Comput. Coupling Phase Diagrams Thermochem. **11**, 271 (1987).
[46] J. R. Rice and J.-S. Wang, Mater. Sci. Eng., A **107**, 23 (1989).
[47] H. C. Herper, E. Hoffmann, and P. Entel, Phys. Rev. B **60**, 3839 (1999).
[48] S. Shang, A. Saengdeejing, Z. Mei, D. Kim, H. Zhang, S. Ganeshan, Y. Wang, and Z. Liu, Comput. Mater. Sci. **48**, 813 (2010).
[49] J. Crangle and M. J. C. Martin, Philos. Mag. (1798–1977) **4**, 1006 (1959).
[50] G. Alers, J. Neighbours, and H. Sato, J. Phys. Chem. Solids **13**, 40 (1960).
[51] N. Sandberg, Z. Chang, L. Messina, P. Olsson, and P. Korzhavyi, Phys. Rev. B **92**, 184102 (2015).
[52] M. Levesque, E. Martínez, C.-C. Fu, M. Nastar, and F. Soisson, Phys. Rev. B **84**, 184205 (2011).
[53] G. Y. Guo and H. H. Wang, Chin. J. Phys. **38**, 949 (2000).
[54] T. P. C. Klaver, D. J. Hepburn, and G. J. Ackland, Phys. Rev. B **85**, 174111 (2012).
[55] H. Zhang, B. Johansson, and L. Vitos, Phys. Rev. B **84**, 140411 (2011).
[56] K. Harste, T. Suzuki, and K. Schwerdtfeger, Mater. Sci. Technol. **8**, 23 (1992).
[57] E. A. Owen, E. L. Yates, and A. H. Sully, Proc. Phys. Soc. **49**, 315 (1937).
[58] K. Honda and Y. Shirikawa, Science Reports of the Research Institutes, Tohoku University. Ser. A, Physics, chemistry and metallurgy **1**, 9 (1949).
[59] Y. S. Lim, J. S. Kim, H. P. Kim, and H. D. Cho, J. Nucl. Mater. **335**, 108 (2004).
[60] S. T. Purcell, W. Folkerts, M. T. Johnson, N. W. E. McGee, K. Jager, J. aan de Stegge, W. B. Zeper, W. Hoving, and P. Grünberg, Phys. Rev. Lett. **67**, 903 (1991).
[61] J. P. Hirth and J. Lothe, *Theory of Dislocations* (Wiley, New York, 1982).
[62] J. Yu, X. Lin, J. Wang, J. Chen, and W. Huang, Appl. Surf. Sci. **255**, 9032 (2009).
[63] D. Kandaskalov, D. Monceau, C. Mijoule, and D. Connétable, Surf. Sci. **617**, 15 (2013).
[64] L. Vitos, A. Ruban, H. Skriver, and J. Kollár, Surf. Sci. **411**, 186 (1998).
[65] M. Aldén, H. L. Skriver, S. Mirbt, and B. Johansson, Phys. Rev. Lett. **69**, 2296 (1992).
[66] K. O. E. Henriksson, N. Sandberg, and J. Wallenius, Appl. Phys. Lett. **93**, 191912 (2008).
[67] Z. Lv, F. Dong, Z. Zhou, G. Jin, S. Sun, and W. Fu, J. Alloys Compd. **607**, 207 (2014).
[68] J. J. Han, C. P. Wang, X. J. Liu, Y. Wang, and Z.-K. Liu, J. Phys.: Condens. Matter **24**, 505503 (2012).

[69] J. Xie, L.-D. Teng, N.-X. Chen, and S. Seetharaman, J. Alloys Compd. **420**, 269 (2006).

[70] J. Soler, E. Artacho, J. Gale, A. Garcia, J. Junquera, P. Ordejon, and D. Sanchez-Portal, J. Phys.: Condens. Matter **14**, 2745 (2002).

[71] D. Leguillon, Eur. J. Mech., A **21**, 61 (2002).

[72] H. S. Kim, Mater. Sci. Eng., A **289**, 30 (2000).

[73] D. J. Rasky and F. Milstein, Phys. Rev. B **33**, 2765 (1986).

[74] H. Hong, B. Rho, and S. Nam, Mater. Sci. Eng., A **318**, 285 (2001).

[75] L. Huang (private communication), DEN-Service de Recherches Métallurgiques Appliquées, CEA, Université Paris-Saclay, F-91191, Gif-sur-Yvette Cedex, France.

[76] J. Pokluda, M. Cerný, M. Sob, and Y. Umeno, Prog. Mater. Sci. **73**, 127 (2015).